

InSe-Te van der Waals heterostructures for currentrectification and photodetection

Hao Wang(王昊), Guo-Yu Xian(冼国裕), Li Liu(刘丽), Xuan-Ye Liu(刘轩冶), Hui Guo(郭辉), Li-Hong Bao(鲍丽宏), Hai-Tao Yang(杨海涛), and Hong-Jun Gao(高鸿钧)

Citation: Chin. Phys. B, 2023, 32 (**8**): 087303. DOI: 10.1088/1674-1056/acd2b1
Journal homepage: http://cpb.iphy.ac.cn; http://iopscience.iop.org/cpb

What follows is a list of articles you may be interested in

Diamond/c-BN van der Waals heterostructure with modulated electronic structures

Su-Na Jia(贾素娜), Gao-Xian Li(李高贤), Nan Gao(高楠), Shao-Heng Cheng(成绍恒), and Hong-Dong Li(李红东)
Chin. Phys. B, 2023, 32 (**7**): 077301. DOI: 10.1088/1674-1056/acac10

Gate-controlled localization to delocalization transition of flat band wavefunction in twisted monolayer-bilayer graphene

Siyu Li(李思宇), Zhengwen Wang(王政文), Yucheng Xue(薛禹承), Lu Cao(曹路), Kenji Watanabe, Takashi Taniguchi, Hongjun Gao(高鸿钧), and Jinhai Mao(毛金海)
Chin. Phys. B, 2023, 32 (**6**): 067304. DOI: 10.1088/1674-1056/acc805

Hexagonal boron phosphide and boron arsenide van der Waals heterostructure as high-efficiency solar cell

Yi Li(李依), Dong Wei(魏东), Gaofu Guo(郭高甫), Gao Zhao(赵高), Yanan Tang(唐亚楠), and Xianqi Dai(戴宪起)
Chin. Phys. B, 2022, 31 (**9**): 097301. DOI: 10.1088/1674-1056/ac6b2a

Magnetic proximity effect induced spin splitting in two-dimensional antimonene/Fe_3GeTe_2 van der Waals heterostructures

Xiuya Su(苏秀崖), Helin Qin(秦河林), Zhongbo Yan(严忠波), Dingyong Zhong(钟定永), and Donghui Guo(郭东辉)
Chin. Phys. B, 2022, 31 (**3**): 037301. DOI: 10.1088/1674-1056/ac16c8

Magneto-transport properties of thin flakes of Weyl semiconductor tellurium

Nan Zhang(张南), Bin Cheng(程斌), Hui Li(李惠), Lin Li(李林), and Chang-Gan Zeng(曾长淦)
Chin. Phys. B, 2021, 30 (**8**): 087304. DOI: 10.1088/1674-1056/ac0a5e

---

InSe–Te van der Waals heterostructures for current rectification and photodetection

Hao Wang(王昊)[1,2,†], Guo-Yu Xian(冼国裕)[1,2,†], Li Liu(刘丽)[1], Xuan-Ye Liu(刘轩冶)[1,2], Hui Guo(郭辉)[1,2,3], Li-Hong Bao(鲍丽宏)[1,2,3,§], Hai-Tao Yang(杨海涛)[1,2,3,‡], and Hong-Jun Gao(高鸿钧)[1,2,3]

[1] *Institute of Physics, Chinese Academy of Sciences, Beijing* 100190, *China*
[2] *University of Chinese Academy of Sciences, Chinese Academy of Sciences, Beijing* 100190, *China*
[3] *Songshan Lake Materials Laboratory, Dongguan* 523808, *China*

(Received 20 January 2023; revised manuscript received 19 April 2023; accepted manuscript online 5 May 2023)

As the basis of modern electronics and optoelectronics, high-performance, multi-functional p–n junctions have manifested and occupied an important position. However, the performance of the silicon-based p–n junctions declines gradually as the thickness approaches to few nanometers. The heterojunction constructed by two-dimensional (2D) materials can significantly improve the device performance compared with traditional technologies. Here, we report the InSe–Te type-II van der Waals heterostructures with rectification ratio up to 1.56×10^7 at drain–source voltage of ±2 V. The p–n junction exhibits a photovoltaic and photoelectric effect under different laser wavelengths and densities and has high photoresponsivity and detectivity under low irradiated light power. Moreover, the heterojunction has stable photo/dark current states and good photoelectric switching characteristics. Such high-performance heterostructured device based on 2D materials provides a new way for futural electronic and optoelectronic devices.

Keywords: indium selenium, tellurium, van der Waals heterostructure, transport, photodetection

PACS: 73.40.Ei, 73.40.–c, 73.40.Lq, 72.40.+w **DOI:** 10.1088/1674-1056/acd2b1

1. Introduction

P–n junctions are fundamental building blocks for modern electronic and optoelectronic devices, which can function as logical rectifiers,[1–3] photodetectors[4–6] and photovoltaics.[7–12] The advents of two-dimensional (2D) materials provide a unique material platform to construct atomically thin p–n junctions due to their atomically layered thickness,[13–15] effective electrostatic control[16,17] even at the monolayer limit, and their abundant and thickness-dependent band alignments. Furthermore, 2D materials with different intrinsic doping levels can be vertically/laterally stacked to form vertical/lateral van der Waals heterostructures (vdWHs), which possess atomically sharp interfaces, enabling them to function as various junctions, such as p–n junctions.

Multilayer indium selenium (>17.5 nm InSe) is a direct bandgap semiconductor with a bandgap of ~1.26 eV,[18–20] and each monolayer is composed of four atomic layers stacked in Se–In–In–Se sequences. InSe is a candidate channel material for 2D electronics and optoelectronics among the 2D layered materials because of the fascinating electrical and optoelectrical transport properties with high on–off ratio of $\sim10^{10}$[14,21] and large photoresponsivity and detectivity of 14250 A/W and 1.63×10^{13} Jones[22] under ferroelectrically gating, respectively. Furthermore, due to the high mobility of few-layer InSe, the quantum Hall effect can be observed at low temperature,[23] indicating that InSe has significant promise for next-generation electronic devices.

As a traditional semiconductor with p-type transport behavior, tellurium (Te) has drawn great attention in the field of electronic devices due to its high hole mobility and excellent photoelectric properties. High-quality and air-stable Te flakes can be prepared by solution synthesis[24,25] for field-effect transistors (FET). Moreover, the band structure of Te is thickness-controlled, which can be tuned from indirect bandgap of 0.35 eV in the bulk to a direct bandgap of 1.04 eV in the monolayer.[25] This tunable band diagram makes Te possesses more appealing properties for applications in electronic and optoelectronic devices.

Here we demonstrate the InSe–Te vdWHs device with rectification behavior and photoelectrical characteristics. The vdWHs device has large rectification ratio reaching 1.56×10^7. The device also has response to laser with different wavelengths and has obvious photo to dark current switching characteristics. Moreover, the p–n junction also has an excellent photodetective behavior with the photoresponsivity up to 0.07 A/W and detectivity approximately to 3.73×10^{15} Jones, and the photovoltaic behavior with an optical-to-electrical conservation of 0.91% and a photovoltaic responsivity of 5.72×10^9 V/W under a light power of 72.11 nW. The InSe–Te based vdWHs device exhibits excellent properties and may enable various applications in futural electronics and optoelectronics.

[†]These authors contribute equally.
[‡]Corresponding author. E-mail: htyang@iphy.ac.cn
[§]Corresponding author. E-mail: lhbao@iphy.ac.cn

© 2023 Chinese Physical Society and IOP Publishing Ltd

2. Results and discussion

Figure 1(a) shows the schematic structure of InSe–Te vdWHs device, where Te and InSe nanoflakes are defined as drain and source electrodes, respectively. Figure 1(b) is the optical image of the fabricated device, in which Te was placed on SiO_2/Si substrate firstly by the wet transfer method, then Pd/Au electrodes were deposited by electron beam deposition (EBD) after standard electron beam lithography (EBL) method to achieve p-type behavior.[25] After that, InSe was exfoliated and stacked with PDMS by dry transfer method[21,22] on top of the Te nanoflake. Cr/Au electrodes were defined by EBL method followed by EBD. InSe can form a good ohmic contact with the Cr/Au contact electrode.[26] Detailed device fabrications are provided in methods. The detailed height profiles of InSe and Te nanoflakes are measured by atomic force microscopy (AFM), the typical heights of InSe and Te nanoflakes are 20 nm–25 nm and 50 nm–60 nm, respectively, as shown in supplementary Fig. S1. The quality of each layer is defined by Raman spectrum, as shown in Fig. 1(c). The Raman peaks of InSe are located at 114 cm^{-1}, 178 cm^{-1} and 227 cm^{-1}, corresponding to A^1_{1g}, E^1_{2g} and A^2_{1g} modes, respectively. For the Te nanoflake, the Raman peaks are located at 89 cm^{-1}, 117 cm^{-1} and 137 cm^{-1}, which are consistent with E_1, A_1 and E_2 modes and similar to previous reports for Te nanoflakes.[18] The Raman peaks in the overlapped region are consistent with individual InSe and Te flakes. To further investigate the quality of the transferred Te flake on SiO_2/Si substrate, Raman mapping at room temperature is performed as shown in Fig. 1(d). The Raman spectrum of the A_1 vibrational mode corresponding to bond bending has good homogeneity, further proving the quality of our transferred Te nanoflakes. We also perform Raman mapping of the heterostructured device, and the uniform distribution of each nanoflake has been demonstrated in supplementary Fig. S2.

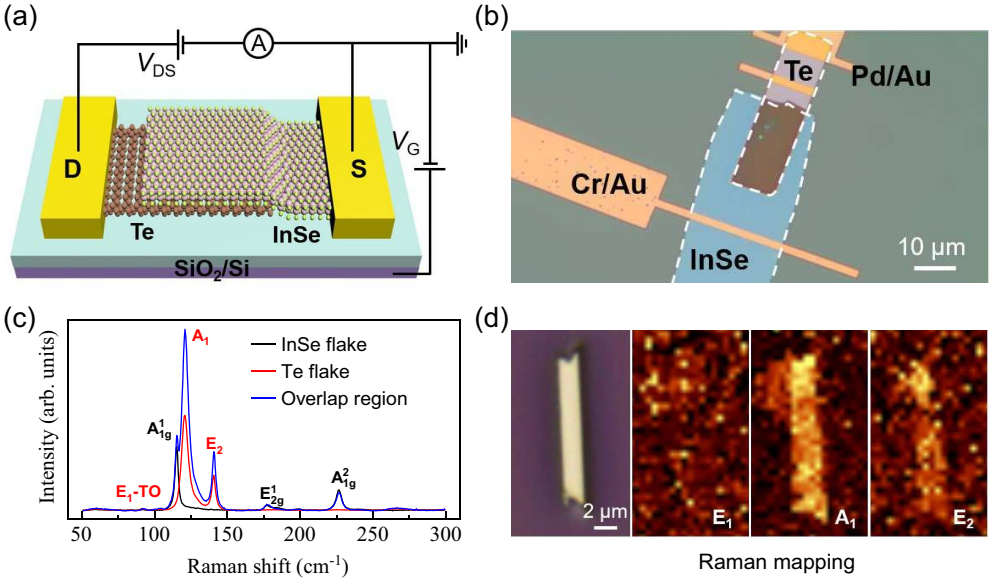


Fig. 1. Device structure and Raman characterizations of the InSe–Te heterostructure. (a) Schematic of the InSe–Te heterostructured device. (b) Optical image of the InSe–Te device placed on a SiO_2/Si substrate. (c) Raman characterization of the InSe–Te heterostructure, in which black, red and blue lines represent InSe nanoflake, Te flake and the overlapped region, respectively. Raman peaks at 115 cm^{-1}, 178 cm^{-1} and 227 cm^{-1} correspond to the A^1_{1g}, E^1_{2g} and A^2_{1g} modes of the InSe flake, respectively. Raman peaks at 89 cm^{-1}, 117 cm^{-1} and 137 cm^{-1} correspond to the E_1, A_1 and E_2 modes for the Te flake, respectively. (d) Raman mapping of the Te nanoflake transferred on SiO_2/Si substrate, indicating the good uniformity of the transferred Te nanoflake.

In order to verify the electrical properties of transferred nanoflakes, we first perform electrical transport measurements on InSe and Te nanoflake, respectively. Figure 2(a) is the transfer curve of the individual InSe flake with gate voltage (V_G) ranging from −60 V to 60 V at drain–source voltage (V_{DS}) = 0.1 V. Source–drain current (I_{DS}) increases as the V_G increases, showing the typical n-type transport behavior. The field-effect mobility (μ_{FE}) is extracted from the linear region of the transfer curve by the following equation including a series of parameters:

$$\mu_{FE} = \frac{L}{W}\frac{1}{C_i}\frac{1}{V_{DS}}\frac{dI_{DS}}{dV_G}, \quad (1)$$

where L and W are the effective channel length and width of the InSe flake, respectively. C_i is the capacitance of 300 nm SiO_2 dielectric. The calculated μ_{FE} of individual InSe nanoflake is 251.1 $cm^2 \cdot V^{-1} \cdot s^{-1}$. Both the trapping charges and the thickness of the dielectric layer could affect the mobility and subthreshold of the device. Inserting a layer of hexagonal boron nitride (hBN) can greatly enhance the mobility of the device due to its atomic flatness, compatible interface and less charge trapping states.[21] Figure 2(b) shows the output curve of the InSe flake from −60 V to 60 V gate range with a 10 V voltage step at 0.1 V V_{DS} range. The good linear behavior indicates the Ohmic contact at InSe and Cr/Au

interfaces. Figure 2(c) shows the transfer curve of the individual Te nanosheet with V_G ranging from −60 V to 60 V at $V_{DS} = 0.1$ V, showing the typical p-type transport behavior. Figure 2(d) also shows the output curve of the individual Te nanoflake from −60 V to 60 V gate range with a 10 V voltage step at 2 V V_{DS} range. Different from the electrical transport properties of the InSe flake, Te with Pd/Au electrodes exhibit distinct p-type electrical transport characteristics. We also perform the electrical performance of Te nanoflake with different contact electrodes (Cr, Ni and Pd), as shown in supplementary Fig. S3, in which only the Pd electrode has formed a good ohmic contact with Te nanoflake.

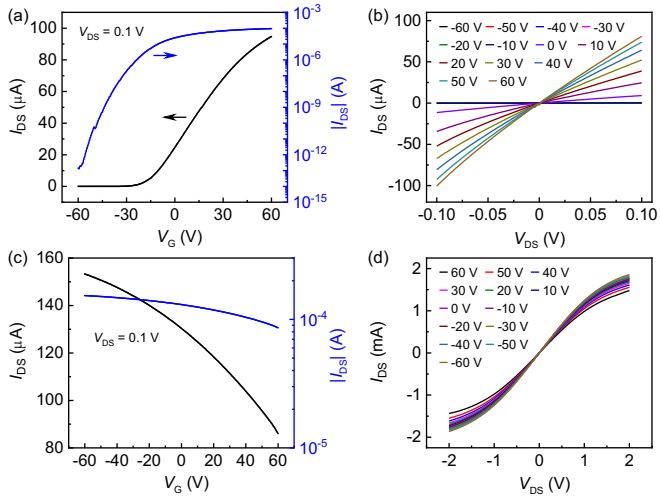


Fig. 2. Electrical transport characterizations of InSe and transferred Te nanoflakes. Panels (a) and (c) are transfer curves of the individual multilayer InSe and Te. Panels (b) and (d) are output curves of the individual multilayer InSe and Te with a gate voltage step of 10 V, indicating a good Ohmic contact between InSe and Cr/Au, Te and Pd/Au electrodes, respectively.

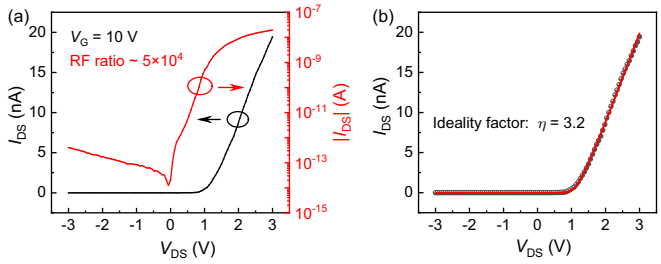


Fig. 3. Electrical transport properties of the InSe–Te vdWHs device. (a) Output curves of the InSe–Te vdWHs device, black and red curves represent the linear and logarithmic coordinate, respectively. (b) Linear plot of the I_{DS}–V_{DS} curve across the p–n junction. The fitting curve (red line) based on a modified Shockley equation is consistent with the experimental result (black balls).

To verify the Fermi level of InSe and Te nanoflakes, surface potential of the heterojunction is measured by Kelvin probe force microscopy (KPFM). The surface potential distribution of the multilayer InSe–Te heterojunction is shown in supplementary Fig. S4(a), where the work function of InSe is 77.7 meV lower than that of Te (supplementary Fig. S4(b)), indicating that electrons can be transferred from InSe into the multilayer Te, thereby establishing a built-in electric field at the deleption region. Supplementary Fig. S4(c) is an ideal band structure diagram for InSe and Te, where the electron affinity energy and band gap of InSe/Te are approximately 4.60 eV[20,27]/4.51 eV[28] and 1.26 eV[19]/0.35 eV[29], respectively. Therefore, the band structure of the InSe–Te van der Waals heterojunction is the staggered type II, which also provides a theoretical basis for the basic properties of p–n junctions, such as rectification, photovoltaics and solar cells, which will be introduced later.

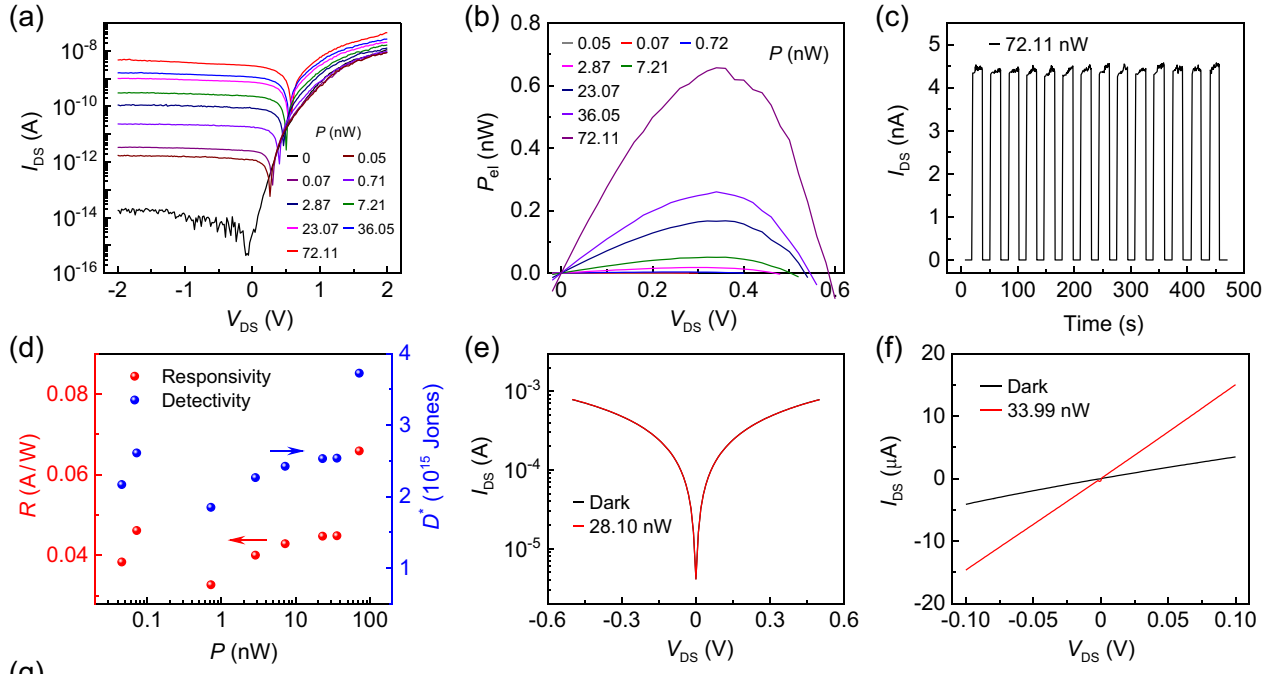
To characterize the electrical transport properties of InSe–Te vdWHs device, output curves are measured at $V_G = 10$ V. Figure 3(a) shows the I_{DS}–V_{DS} curves of the transferred InSe–Te heterojunction on SiO_2/Si substrate. The multilayer InSe–Te vdWHs device shows a strong current rectifying behavior with a large rectification ratio approximately 5×10^4 at 3 V V_{DS} range, proving the stable rectifying behavior of the InSe–Te type II heterojunction. This vdWHs device with high rectification ratio is suitable for constructing rectifiers and logic devices.[1] The p–n junction can be fitted with a modified Shockley equation, including a series of resistance R_s,[1,30]

$$I_D = \frac{\eta V_T}{R_S} W\left[\frac{I_0 R_S}{\eta V_T}\exp\left(\frac{V_D + I_0 R_S}{\eta V_T}\right)\right] - I_0, \tag{2}$$

where η, V_T, W, I_0 refers to ideality factor, the thermal voltage $(k_B T/e)$ at temperature T, lambert W function and reverse-bias current, respectively. k_B and e are the Boltzmann constant and the electron charge, respectively. The fitting curve is fully consistent with the experimental data as shown in Fig. 3(b), which confirms the formation of the p–n junction. The transport mechanism across the p–n junction can be revealed by the value of the ideality factor (η). The typical ideality factor for our InSe–Te p–n junction is extracted as ~ 3.2, which demonstrates that the transport mechanism is dominated by the recombination process.[30] We also perform the rectifying characteristics under different V_G ranging from −30 V to 30 V with a 10 V voltage step at 2 V V_{DS} range as shown in supplementary Fig. S5(a), the on-state current gradually increases with the increase of V_G, and the off-state current remains basically unchanged with the increase of the gate voltage, which is due to the gradually enhanced n-type behavior of InSe nanoflake and basically unchanged p-type behavior of Te as V_G increases. Supplementary Fig. S5(b) shows the rectification ratio of the device corresponding to each V_G, which can reach up to 1.56×10^7 at V_{DS} of ±2 V under $V_G = 30$ V, demonstrating that our device is suitable for designing logic rectifiers. Electrical characteristics of other devices with the same device structure are also performed as shown in supplementary Fig. S6, the device achieves a large rectification ratio up to 3.45×10^6 at V_{DS} of ±2 V under $V_G = 10$ V, demonstrat-

ing that the InSe–Te heterostructured device is universal and reproducible. In addition, we implement the electrical performance of InSe nanoflake-Te nanowire as shown in supplementary Fig. S7, in which a rectification ratio of 401.8 at V_{DS} of ± 3 V under $V_G = -5$ V can be observed, the rectification ratio is much smaller than that of InSe–Te nanoflakes, which may due to the thinner Te nanowire induced smaller deleption region of the formed p–n junction.

When a photon with sufficient energy strikes the p–n junction, a pair of free electron and hole could be generated and separated in the depletion region due to the built-in electric field, such mechanism is known as the photovoltaic and photoelectric effect, which can be used as photovoltaic cells and photodiode in practical applications. Here we characterize the photoresponse properties of the InSe–Te vdWHs device using laser with different wavelengths and intensities. All the photoresponse properties of the InSe–Te heterojunction are measured at $V_G = 10$ V unless otherwise specified. Figure 4(a) shows the output curve of the InSe–Te vdWs device under dark and laser irradiation with different powers at the laser wavelength of 450 nm. The device has a positive open-circuit voltage (V_{OC}) and a negative short-circuit current (I_{SC}) under the laser irradiation. V_{OC} and I_{SC} increase as the laser power increases and reach the maximum at the laser power of 72.11 nW, demonstrating that the InSe–Te vdWs device can be used in photovoltaic cells and photoelectric detections. Figure 4(b) shows the P_{el} ($P_{el} = V_D \times I_D$) varies with V_{DS}, and $P_{el,max}$ is located at ~ 0.34 V, which is the most suitable voltage position for InSe–Te photovoltaic cell to obtain maximum output efficiency. Figure 4(c) shows the time-evolution of InSe–Te p–n junction at $V_{DS} = -2$ V under dark and the laser power of 72.11 nW, the device has obvious light-to-dark current switching behaviour, which indicates that InSe–Te heterostructure has the ability of light detection.



(g)

Laser power (nW)	0.05	0.07	0.71	2.87	7.21	23.07	36.05	72.11
V_{OC} (V)	0.26	0.29	0.40	0.46	0.50	0.53	0.55	0.58
Fill factor	0.40	0.43	0.45	0.45	0.43	0.42	0.41	0.39
Efficiency (%)	0.28	0.43	0.45	0.62	0.70	0.72	0.72	0.91
Responsivity (10^8 V/W)	57.23	40.21	5.54	1.60	0.69	0.23	0.15	0.08

Fig. 4. Photoelectrical performance of the InSe–Te vdWHs device under 450 nm laser irradiation. (a) Output curves of the InSe–Te heterostructure in dark and under 450 nm light illumination with different power levels. (b) P_{el} as a function of V_{DS} under different laser powers. (c) Photocurrent of the InSe–Te heterostructure with 72.11 nW laser power at $V_{DS} = -2$ V. (d) Photoresponsivity and detectivity versus laser power under the 450 nm laser wavelength. (e) Output curves of the Te nanoflake in dark and with 28.10 nW laser power at $V_{DS} = -2$ V. (f) Output curves of the InSe nanoflake in dark and with 33.99 nW laser power at $V_{DS} = -2$ V. (g) Optoelectronic properties of the InSe–Te heterostructure at different laser power levels, including V_{OC}, FF, η_{EPCE} and responsivity, respectively.

To further evaluate the photoelectrical properties of InSe–Te heterojunction, responsivity (R) and detectivity (D^*) are extracted by the following equations:[22]

$$R = \frac{I_{\rm ph}}{P \times S}, \tag{3}$$

$$D^* = \frac{RS^{1/2}}{(2eI_{\rm d})^{1/2}}, \tag{4}$$

where $I_{\rm ph}$, P, S, e, $I_{\rm d}$ are photocurrent ($I_{\rm ph} = I_{\rm light} - I_{\rm dark}$), laser power density, the effective channel excitation area, electron charge and dark current, respectively. Figure 4(d) shows the calculated R and D^* of the InSe–Te vdWHs device illuminated by 450 nm laser at $V_{\rm DS}$ of -2 V as a function of light power. The photodiode exhibits a photoresponsivity 0.07 A/W and a high detectivity up to 3.73×10^{15} Jones when the incident power is 72.11 nW. The detectivity is much higher than the previous reported value of 1.1×10^{13} Jones[18] because of the sufficiently low dark current at $V_{\rm DS} = -2$ V. In order to exclude the influence of Te and InSe nanoflakes of the heterojunction, we perform photoelectrical characterizations on the separate Te and the separate InSe nanoflake as shown in Figs. 4(e) and 4(f), respectively. There is no $I_{\rm SC}$ for individual Te and InSe nanoflakes at zero bias, indicating that the photovoltaic effect of the heterojunction only occurs in the depletion region of the p–n junction rather than in each independent area. The $V_{\rm OC}$, fill factor (FF $= P_{\rm el,max}/I_{\rm SC} \times V_{\rm OC}$), electrical power conversion efficiency ($\eta_{\rm EPCE} = P_{\rm el,max}/P_{\rm laser}$) and photovoltage responsivity ($V_{\rm OC}/P_{\rm laser}$) are also extracted as shown in Fig. 4(g). An overall $\eta_{\rm EPCE}$ of 0.91% and photovoltage responsivity of 5.72×10^9 V/W at the laser power of 72.11 nW is achieved. We also perform the photoelectrical performance of the InSe–Te heterostructured device under laser wavelengths of 532 nm and 633 nm as shown in supplementary Figs. S8 and S9, respectively, showing the similar electrical performance compared with the device under 450 nm, which indicates that our device is suitable for the detection of visible light.

To explore the light-to-dark current switching characteristics of the InSe–Te heterostructured device, we measure the photoresponse speed of the heterojunction under the wavelength of 450 nm at $V_{\rm DS} = -2$ V, as shown in supplementary Fig. S10. The response time of the individual rise and fall process are 340 μs and 650 μs, respectively, demonstrating that our InSe–Te heterojunction has the ability for fast responding speed.

3. Methods

Device fabrication and electrical characterization Te nanoflakes and Te nanowires were grown in a three-zone furnace by atmospheric pressure physics vapor deposition (PVD). The Te lump was placed in the first zone while the mica was held in the second zone which was parallel to the quartz tube. The precursors and the mica substrate were heated to a few hundred degrees and cooled down to room temperature naturally after the end of the growth. The growth process was performed in a hydrogen–argon mixture gas atmosphere. InSe bulk crystals were purchased from 2D semiconductors. InSe was exfoliated by 3M scotch in the glovebox. InSe nanoflake stacked on PDMS was transferred onto Te nanoflake by the dry transfer method. 6/60 nm Cr/Au and 15/85 nm Pd/Au were defined by standard electron-beam lithography and evaporated by electron-beam evaporation following with lift-off procedure. Electrical measurements were performed with a Keithley 4200 semiconductor characterization system (4200-SCS) in a vacuum probe station at room temperature.

4. Conclusion

We have fabricated InSe–Te vdWHs device to achieve multiple functions on a single device. InSe and Te nanoflakes exhibit excellent n-type and p-type transport behavior individually. The heterostructured InSe–Te p–n junction has a large rectification ratio of 1.56×10^7 at a relatively low $V_{\rm DS}$ of ± 2 V. In addition, the p–n junction has photovoltaic and photoelectric effects, with a high conversion efficiency of up to 0.91% and a photovoltage responsivity up to 5.72×10^9 V/W under the wavelength of 450 nm with an incident power of 72.11 nW, and a photocurrent responsivity of 0.07 A/W and a detectivity of 3.73×10^{15} Jones. In addition, the heterojunction also has the photovoltaic and photoelectric characteristics and light-to-dark switching behavior under different laser wavelengths, which can be implemented in the detection of visible light. Our work provides a new opportunity for the development of futural electronic and optoelectronic devices.

Acknowledgments

Project supported by the Ministry of Science and Technology of China (Grant No. 2018YFA0305800), the National Natural Science Foundation of China (Grant No. 61888102), and the Chinese Academy of Sciences (Grant Nos. ZDBS-SSW-WHC001, XDB33030100, XDB30000000, and YSBR-003).

References

[1] Li D, Chen M Y, Sun Z Z, Yu P, Liu Z, Ajayan P M and Zhang Z X 2017 *Nat. Nanotechnol.* **12** 901

[2] Cheng R, Yin L, Wang F, Wang Z, Wang J, Wen Y, Huang W, Sendeku M G, Feng L, Liu Y and He J 2019 *Adv. Mater.* **31** 1901144

[3] Pan C, Wang C Y, Liang S J, Wang Y, Cao T, Wang P, Wang C, Wang S, Cheng B, Gao A, Liu E, Watanabe K, Taniguchi T and Miao F 2020 *Nat. Electron.* **3** 383

[4] Bie Y Q, Grosso G, Heuck M, Furchi M M, Cao Y, Zheng J, Bunandar D, Navarro-Moratalla E, Zhou L, Efetov D K, Taniguchi T, Watanabe K, Kong J, Englund D and Jarillo-Herrero P 2017 *Nat. Nanotechnol.* **12** 1124

[5] Sun J C, Wang Y Y, Guo S Q, Wan B S, Dong L Q, Gu Y D, Song C, Pan C F, Zhang Q H, Gu L, Pan F and Zhang J Y 2020 *Adv. Mater.* **32** 1906499

[6] Huo N and Konstantatos G 2017 *Nat. Commun.* **8** 572

[7] Deng Y X, Luo Z, Conrad N J, Liu H, Gong Y J, Najmaei S, Ajayan P M, Lou J, Xu X F and Ye P D 2014 *ACS Nano* **8** 8292

[8] Wu G J, Wang X D, Chen Y, Wu S Q, Wu B M, Jiang Y Y, Shen H, Lin T, Liu Q, Wang X R, Zhou P, Zhang S T, Hu W D, Meng X J, Chu J H and Wang J L 2020 *Adv. Mater.* **32** 1907937

[9] Furchi M M, Pospischil A, Libisch F, Burgdorfer J and Mueller T 2014 *Nano Lett.* **14** 4785

[10] Wu G, Tian B, Liu L, Lv W, Wu S, Wang X, Chen Y, Li J, Wang Z, Wu S, Shen H, Lin T, Zhou P, Liu Q, Duan C, Zhang S, Meng X, Wu S, Hu W, Wang X, Chu J and Wang J 2020 *Nat. Electron.* **3** 43

[11] Baugher B W H, Churchill H O H, Yang Y and Jarillo-Herrero P 2014 *Nat. Nanotechnol.* **9** 262

[12] Lee C H, Lee G H, van der Zande A M, Chen W, Li Y, Han M, Cui X, Arefe G, Nuckolls C, Heinz T F, Guo J, Hone J and Kim P 2014 *Nat. Nanotechnol.* **9** 676

[13] Geim A K and Grigorieva I V 2013 *Nature* **499** 419

[14] Wu L, Wang A, Shi J, Yan J, Zhou Z, Bian C, Ma J, Ma R, Liu H, Chen J, Huang Y, Zhou W, Bao L, Ouyang M, Pennycook S J, Pantelides S T and Gao H J 2021 *Nat. Nanotechnol.* **16** 882

[15] Li M Y, Shi Y, Cheng C C, Lu L S, Lin Y C, Tang H L, Tsai M L, Chu C W, Wei K H, He J H, Chang W H, Suenaga K and Li L J 2015 *Science* **349** 524

[16] Desai S B, Madhvapathy S R, Sachid A B, Llinas J P, Wang Q, Ahn G H, Pitner G, Kim M J, Bokor J, Hu C, Wong H S P and Javey A 2016 *Science* **354** 99

[17] Wu F, Tian H, Shen Y, Hou Z, Ren J, Gou G, Sun Y, Yang Y and Ren T L 2022 *Nature* **603** 259

[18] Qin F, Gao F, Dai M, Hu Y, Yu M, Wang L, Feng W, Li B and Hu P 2020 *ACS Appl. Mater. Interfaces* **12** 37313

[19] Lv Q, Yan F, Mori N, Zhu W, Hu C, Kudrynskyi Z R, Kovalyuk Z D, Patane A and Wang K 2020 *Adv. Funct. Mater.* **30** 1910713

[20] Mudd G W, Svatek S A, Ren T, Patane A, Makarovsky O, Eaves L, Beton P H, Kovalyuk Z D, Lashkarev G V, Kudrynskyi Z R and Dmitriev A I 2013 *Adv. Mater.* **25** 5714

[21] Wu L M, Shi J A, Zhou Z, Yan J H, Wang A W, Bian C, Ma J J, Ma R S, Liu H T, Chen J C, Huang Y, Zhou W, Bao L H, Ouyang M, Pantelides S T and Gao H J 2020 *Nano Res.* **13** 1127

[22] Liu L, Wu L, Wang A, Liu H, Ma R, Wu K, Chen J, Zhou Z, Tian Y, Yang H, Shen C, Bao L, Qin Z, Pantelides S T and Gao H J 2020 *Nano Lett.* **20** 6666

[23] Bandurin D A, Tyurnina A V, Yu G L, Mishchenko A, Zolyomi V, Morozov S V, Kumar R K, Gorbachev R V, Kudrynskyi Z R, Pezzini S, Kovalyuk Z D, Zeitler U, Novoselov K S, Patane A, Eaves L, Grigorieva I V, Fal'ko V I, Geim A K and Cao Y 2017 *Nat. Nanotechnol.* **12** 223

[24] Amani M, Tan C, Zhang G, Zhao C, Bullock J, Song X, Kim H, Shrestha V R, Gao Y, Crozier K B, Scott M and Javey A 2018 *ACS Nano* **12** 7253

[25] Wang Y, Qiu G, Wang R, Huang S, Wang Q, Liu Y, Du Y, Goddard W A III, Kim M J, Xu X, Ye P D and Wu W 2018 *Nat. Electron.* **1** 228

[26] Feng W, Zhou X, Tian W Q, Zheng W and Hu P A 2015 *Phys. Chem. Chem. Phys.* **17** 3653

[27] Wu F, Xia H, Sun H, Zhang J, Gong F, Wang Z, Chen L, Wang P, Long M, Wu X, Wang J, Ren W, Chen X, Lu W and Hu W 2019 *Adv. Funct. Mater.* **29** 1900314

[28] Niles D W, Li X, Sheldon P and Höchst H 1995 *J. Appl. Phys.* **77** 4489

[29] Peng M, Yu Y, Wang Z, Fu X, Gu Y, Wang Y, Zhang K, Zhang Z, Huang M, Cui Z, Zhong F, Wu P, Ye J, Xu T, Li Q, Wang P, Yue F, Wu F, Dai J, Chen C and Hu W 2022 *ACS Photonics* **9** 1775

[30] Banwell T C and Jayakumar A 2000 *Electron. Lett.* **36** 291